

**Significant reduction of the lattice thermal conductivity in antiferrofluorites via a split-anion approach**Shi-ming Liu,<sup>1</sup> Jun-jie Shi<sup>1,\*</sup>, Yao-hui Zhu,<sup>2</sup> Wen-hui Guo,<sup>1</sup> Yong He,<sup>1</sup> Chong Tian,<sup>1</sup> Xinqiang Wang,<sup>1</sup> and Hong-xia Zhong<sup>3,†</sup><sup>1</sup>State Key Laboratory for Artificial Microstructures and Mesoscopic Physics, School of Physics, Peking University Yangtze Delta Institute of Optoelectronics, Peking University, Beijing 100871, China<sup>2</sup>Physics Department, Beijing Technology and Business University, Beijing 100048, China<sup>3</sup>School of Mathematics and Physics, China University of Geosciences, Wuhan 430074, China

(Received 2 January 2023; accepted 27 April 2023; published 31 May 2023)

Searching for thermoelectrics with low lattice thermal conductivity  $\kappa_l$  is crucial to address needs for waste heat recovery, but few light element dominated materials provide a low  $\kappa_l$ . Herein, we propose an effective strategy, i.e., a split-anion approach, to reduce the  $\kappa_l$  of the antiferrofluorite. After introducing the split-anion approach, the stable quasiantiferrofluorite  $\text{Li}_4\text{OSe}$  is obtained, and  $\kappa_l$  is reduced by  $\sim 90\%$  compared to the antiferrofluorite  $\text{Li}_2\text{Se}$ . The  $\kappa_l$  value of  $\text{Li}_4\text{OSe}$  reaches as low as  $0.49\text{--}1.75 \text{ W m}^{-1} \text{ K}^{-1}$ , the range of thermoelectric applications, despite numerous light Li atoms and a large mass mismatch among the constituent atoms. This significant reduction of the thermal conductivity mainly results from the soft phonon branches and large optical bandwidth induced by lattice symmetry breaking after the split-anion approach. These findings offer ample scope for tuning the phonon band structure and thermal transport by reducing lattice symmetry like in the split-anion approach, leading to ultralow  $\kappa_l$  of materials.

DOI: [10.1103/PhysRevB.107.205206](https://doi.org/10.1103/PhysRevB.107.205206)**I. INTRODUCTION**

Low lattice thermal conductivity plays a fundamental role in waste heat recovery, data storage, and thermal barrier coatings. According to Slack's rule [1], elements with a heavy atom mass are always adopted, such as  $\text{Bi}_2\text{Te}_3$ ,  $\text{Sb}_2\text{Te}_3$ ,  $\text{SnTe}$ , and  $\text{GeTe}$  [2,3]. Recently, some exciting mechanisms of low lattice thermal conductivity were also suggested, including lone pair electrons [4,5], chemical bond hierarchy [6], resonant bonding [7,8], and metavalent bonding [9], which are deepening our physical understanding of thermal transport in solids. However, light elements like Li, C, and Si have rarely been selected for low lattice thermal conductivity materials, even though they are more environmentally friendly and abundant on earth. The important reasons are that compounds composed of light elements usually have extremely high phonon group velocities and relatively weak phonon scattering [10,11].

The antiferrofluorites  $\text{Li}_2\text{X}$  ( $X = \text{Se}$  and  $\text{Te}$ ) are typical kinds of compounds with a large mass mismatch among constituent atoms, in which the crystals not only have tightly bunched acoustic branches and low acoustic phonon group velocities, determined by the heavier element [12], but also possess large proportions of light elements. The antiferrofluorites  $\text{Li}_2\text{X}$  have wide bandwidth and dispersive optical branches, inducing strong interactions of one acoustic phonon with two optical phonons (*ao* scattering), which are the dominant resistance to heat-carrying acoustic phonons [12]. However, the

large frequency gap between acoustic phonons and optical phonons (*a-o* gap), determined by mass mismatch among constituent atoms [12,13], inhibits the interaction of two acoustic phonons with an optical phonon (*ao* scattering) and thus leads to the awkward thermal conductivities in  $\text{Li}_2\text{X}$ , i.e.,  $14.9 \text{ W m}^{-1} \text{ K}^{-1}$  for  $\text{Li}_2\text{Se}$  and  $12.5 \text{ W m}^{-1} \text{ K}^{-1}$  for  $\text{Li}_2\text{Te}$  [12]. At present, the antiferrofluorites  $\text{Li}_2\text{X}$  with  $\kappa_l > 10 \text{ W m}^{-1} \text{ K}^{-1}$  [12,14] do not have the same excellent thermoelectric (TE) performance as traditional materials, whose thermal conductivities are generally less than  $5 \text{ W m}^{-1} \text{ K}^{-1}$ , for example,  $1.2 \text{ W m}^{-1} \text{ K}^{-1}$  for  $\text{Bi}_2\text{Te}_3$ ,  $1.9 \text{ W m}^{-1} \text{ K}^{-1}$  for  $\text{Sb}_2\text{Te}_3$ , and  $3.1 \text{ W m}^{-1} \text{ K}^{-1}$  for  $\text{Bi}_2\text{Se}_3$  [2]. It is therefore imperative to provide a strategy to remove the *a-o* gap and reduce the thermal conductivity in antiferrofluorite crystals to realize a brand-new class of TE materials with a large mass mismatch among constituent atoms.

In this work, we provide an effective strategy, i.e., the split-anion approach, to reduce the lattice thermal conductivity of the antiferrofluorite. For instance,  $\text{Li}_2\text{Se}$  will transform to the quasiantiferrofluorite  $\text{Li}_4\text{OSe}$ , in which the introduction of the O atom lowers the lattice asymmetry and removes the *a-o* gap. Although  $\text{Li}_4\text{OSe}$  is a compound with many Li and O atoms, low thermal lattice conductivity, ranging from  $1.75 \text{ W m}^{-1} \text{ K}^{-1}$  at 300 K to  $0.49 \text{ W m}^{-1} \text{ K}^{-1}$  at 1000 K, can be obtained due to the anomalous coupling between acoustic and optical phonons induced by the optical phonon mode softening. Based on a simple asymmetric  $\text{Li}_2\text{Se}$  model, a clear relationship between the soft optical phonon modes and the lattice symmetry breaking is uncovered. We further provide evidence that this picture of soft optical phonon modes is universal in other quasiantiferrofluorites, through which light element dominated materials are

\*jjshi@pku.edu.cn

†zhonghongxia@cug.edu.cn

expected to lead to new environmentally friendly and low-cost thermoelectrics.

## II. CALCULATION METHOD

The main calculations based on density functional theory are implemented in the Vienna Ab initio Simulation Package (VASP) [15,16]. The projector augmented wave method is used to describe the electron-ion potential [17]. The plane wave basis set and the generalized gradient approximation with the Perdew-Burke-Ernzerhof functional are used [18]. A  $15 \times 15 \times 15$  Monkhorst-Pack  $k$ -point mesh [19] is employed to sample the Brillouin zone for self-consistent calculation. The kinetic energy cutoff is set to 600 eV in all calculations. The convergence tolerances of the energy and force are smaller than  $10^{-4}$  eV/Å and  $10^{-8}$  eV.

To discuss phonon transport, we adopt the SHENGBTE code [20], which can provide accurate  $\kappa_l$  values with good agreement with the experimental result [21]. The second- and third-order interatomic force constants are computed using the PHONOPY and THIRDDORDER packages [20,22–24], respectively, as inputs of the SHENGBTE code. In the linearized phonon Boltzmann transport equation (BTE),  $\kappa_l$  is calculated as

$$\kappa_l^{\alpha\beta} = \frac{1}{k_B T^2 N V} \sum_{\lambda} f_{\lambda}^0 (f_{\lambda}^0 + 1) (\hbar \omega_{\lambda})^2 v_{\lambda}^{\alpha} F_{\lambda}^{\beta}, \quad (1)$$

$$\begin{aligned} \Sigma''_{n\mathbf{k}}(\omega, T) = & \pi \sum_{mv} \int_{\text{BZ}} \frac{d\mathbf{q}}{\Omega_{\text{BZ}}} |g_{mn,v}(\mathbf{k}, \mathbf{q})|^2 \{ [n_{\mathbf{q}v}(T) + f_{m\mathbf{k}+\mathbf{q}}(T)] \delta(\omega - (\varepsilon_{m\mathbf{k}+\mathbf{q}} - \varepsilon_F) + \omega_{\mathbf{q}v}) \\ & + [n_{\mathbf{q}v}(T) + 1 - f_{m\mathbf{k}+\mathbf{q}}(T)] \delta[\omega - (\varepsilon_{m\mathbf{k}+\mathbf{q}} - \varepsilon_F) - \omega_{\mathbf{q}v}] \}, \end{aligned} \quad (3)$$

where  $g_{mn,v}(\mathbf{k}, \mathbf{q})$  is the matrix element of one  $e$ -ph interaction process involving the given phonon and two electrons (or holes) with band indices  $m$  and  $n$  and wave vectors  $\mathbf{k}$  and  $\mathbf{k} + \mathbf{q}$ ,  $n_{\mathbf{q}v}(T)$  is the Bose-Einstein distribution, and  $f_{n\mathbf{k}}(T)$  is the electronic occupation. The lifetime of electrons can be obtained by  $1/\tau_{n\mathbf{k}} = 2\Sigma''_{n\mathbf{k}}/\hbar$ . Meanwhile, the imaginary part of the phonon self-energy can be defined as [34]

$$\begin{aligned} \Pi''_{\mathbf{q}v}(\omega, T) = & 2\pi \sum_{mn} \int_{\text{BZ}} \frac{d\mathbf{k}}{\Omega_{\text{BZ}}} \times |g_{mn,v}(\mathbf{k}, \mathbf{q})|^2 \\ & \times [f_{n\mathbf{k}}(T) - f_{m\mathbf{k}+\mathbf{q}}(T)] \delta(\varepsilon_{m\mathbf{k}+\mathbf{q}} - \varepsilon_{n\mathbf{k}} - \omega). \end{aligned} \quad (4)$$

The phonon lifetime due to the  $e$ -ph interaction ( $1/\tau_{\mathbf{q}v}^{ep}$ ) can be obtained from  $\Pi''_{\mathbf{q}v}$  by  $(1/\tau_{\mathbf{q}v}^{ep}) = (2\Pi''_{\mathbf{q}v}/\hbar)$ . The thermoelectric properties of  $p$ -type  $\text{Li}_4\text{OSe}$  are obtained by using the BOLTZTRAP code [37], with the mode-resolved carrier lifetime from EPW. Refer to the Supplemental Material for details [36].

## III. RESULTS AND DISCUSSION

### A. Crystal structure and stability

As shown in Fig. 1(a), the antifluorite  $\text{Li}_2\text{Se}$  crystallizes in space group  $Fm\bar{3}m$ , in which each Li is fourfold coordinated while each Se is eightfold coordinated [38]. By the split-anion approach, the crystal  $\text{Li}_4\text{OSe}$  is obtained. The structures of

where  $\omega_{\lambda}$  is the phonon frequency of wave vector  $\mathbf{q}$  with a branch index  $\lambda$ ,  $v_{\lambda}$  denotes the group velocity of the phonon, and  $f_{\lambda}^0$  is the Bose-Einstein distribution function for the phonon population.  $F_{\lambda}^{\beta}$  can be expressed as

$$F_{\lambda}^{\beta} = \tau_{\lambda}^0 (v_{\lambda}^{\beta} + \Delta_{\lambda}^{\beta}), \quad (2)$$

where  $\tau_{\lambda}^0$  is the phonon lifetime of the phonon mode  $\lambda$  and  $\Delta_{\lambda}^{\beta}$  is a correction term obtained by the fully iterative solution of the BTE.

We construct the Wannier tight-binding (TB) phonon Hamiltonian from the second-order interatomic force constants as implemented in WANNIERTOOLS [25]. The force constants in phonon TB models are constructed by Slater-Koster TB parameters [26] because the  $x$ ,  $y$ , and  $z$  components for atoms can be regarded as three localized  $p$  orbitals in three-dimensional space [27,28].

Electron-phonon ( $e$ -ph) interactions are important for carrier and phonon transport [29,30]. We consider the  $e$ -ph interaction by using the QUANTUM ESPRESSO and Electron-phonon Wannier (EPW) codes [31–35]. The electronic wave functions are calculated using a dense  $15 \times 15 \times 15$   $k$ -point grid within the EPW code in order to perform the Wannier interpolation. The Wannier interpolated band structure is shown in Fig. S13 in the Supplemental Material [36]. The imaginary part of the electron self-energy  $\Sigma''_{n\mathbf{k}}$  is expressed as [34]

$\text{Li}_4\text{OSe}$  along different crystal planes are shown in Fig. 1(b). We can see that one Se anion in the crystal coordinates with eight Li cations, which is similar to that in the antifluorite  $\text{Li}_2\text{Se}$ , while O anions are in fourfold coordination.  $\text{Li}_4\text{OSe}$

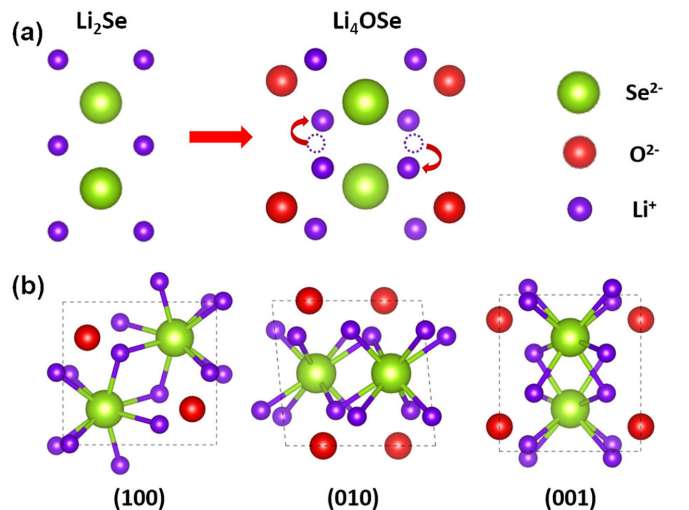


FIG. 1. (a) Structural change from the antifluorite  $\text{Li}_2\text{Se}$  to the quasiantifluorite  $\text{Li}_4\text{OSe}$  with space group  $P2/c$  along (001) crystal planes. (b) Crystal structure of the quasiantifluorite  $\text{Li}_4\text{OSe}$ .

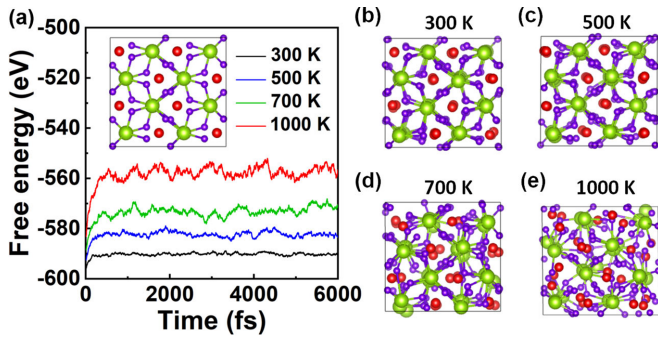


FIG. 2. (a) Evolution of total energy versus simulation time in AIMD for bulk  $\text{Li}_4\text{OSe}$  at 300–1000 K. The inset in (a) is the plane of the  $3 \times 2 \times 2$  supercell at 0 K for  $\text{Li}_4\text{OSe}$ . The corresponding snapshot of the final equilibrium structure after 6000 fs at (b) 300 K, (c) 500 K, (d) 700 K, and (e) 1000 K.

belongs to the monoclinic crystal system, with a space group symmetry of  $P2/c$  and a point group symmetry of  $C_{2D}$ , indicating a lower-symmetry structure than  $\text{Li}_2\text{Se}$  due to the introduction of the O atom. Therefore, we call materials like  $\text{Li}_4\text{OSe}$  “quasiantifluorites.” The x-ray-diffraction patterns of  $\text{Li}_4\text{OSe}$  are calculated with VESTA [39], in which the radiation wavelength is chosen to be  $1.5418 \text{ \AA}$  (Cu  $K\alpha$ ; see Fig. S1(a) in the Supplemental Material [36]).

We evaluate the stability of  $\text{Li}_4\text{OSe}$  from three aspects. We first calculate the phonon spectra and observe no imaginary frequency, suggesting that the crystal is dynamically stable at 0 K. In order to confirm the thermodynamic characteristics of  $\text{Li}_4\text{OSe}$  at finite temperature, we further perform *ab initio* molecular dynamics (AIMD) simulations [40–43], as shown in Fig. 2 and also Fig. S1(b) in the Supplemental Material [36]. In Fig. S1(b), the temperature fluctuations show that the thermostat and ionic movement couple well. A  $3 \times 2 \times 2$  supercell of  $\text{Li}_4\text{OSe}$  at 0 K in Fig. 2(a) is shown for comparison. It is found that the geometries of  $\text{Li}_4\text{OSe}$  are well preserved after 6000 fs at 300–700 K, while some Li cations begin to migrate at 1000 K. The time-dependent evolutions of total energies at 300–1000 K oscillate within a very narrow range in Fig. 2(a), clearly illustrating the high-temperature stability of  $\text{Li}_4\text{OSe}$ . Furthermore, it is known that free energy differences ( $\Delta G = \Delta H - T\Delta S$ , where  $\Delta H$  and  $\Delta S$  are the formation energy and formation entropy, respectively) between compounds and their decomposition products can also reflect their thermodynamic stability. We thus give  $\Delta G$  [44] between  $\text{Li}_4\text{OSe}$  and its competing binary phases, i.e.,  $\text{Li}_2\text{Se}$  [38] and  $\text{Li}_2\text{O}$  [45] (see Fig. S1(c) in the Supplemental Material [36]). The negative value of the free energy differences means that  $\text{Li}_4\text{OSe}$  is thermodynamically stable at 0–1000 K.

### B. Lattice thermal transport property

Generally, the large mismatch in mass among atoms leads to a frequency gap between acoustic and optical phonons (*a-o* gap), such as  $\text{Li}_2\text{Se}$ ,  $\text{BeSe}$ , and  $\text{BeTe}$  [12,13], in which only high-frequency acoustic phonons, localized in a small region of reciprocal space, can participate in the interaction of two acoustic phonons with an optical phonon (*aa* scattering), resulting in a reduced scattering rate and large

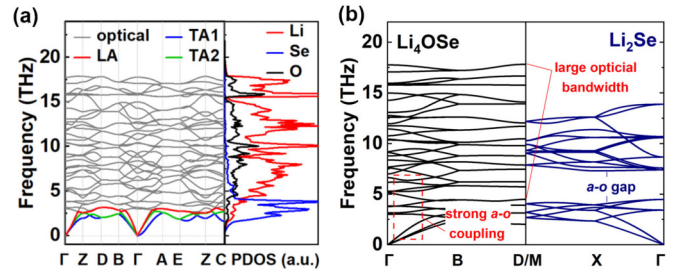


FIG. 3. (a) Calculated phonon spectra (left) and phonon density of states (right) of  $\text{Li}_4\text{OSe}$ . High-symmetry points of the first Brillouin zone are given in Fig. S2 in the Supplemental Material [36]. (b) Comparison of phonon dispersions between  $\text{Li}_4\text{OSe}$  (black curves) and  $\text{Li}_2\text{Se}$  (blue curves) in the same direction. Compared with  $\text{Li}_2\text{Se}$ ,  $\text{Li}_4\text{OSe}$  has strong *a-o* coupling and large optical bandwidth.

thermal conductivity. Nevertheless, this rule cannot be applied to  $\text{Li}_4\text{OSe}$ . We give the phonon spectra and phonon density of states of  $\text{Li}_4\text{OSe}$  in Fig. 3(a) and find that the heat-carrying acoustic phonon modes originate mainly from the heavy Se atoms, while the high-frequency optical phonon modes are dominated by light Li atoms. Surprisingly, the bandwidth of the optical phonon branches is so large that the optical phonons dramatically couple with the acoustic phonons, even though Li and Se atoms have very different masses. In order to intuitively demonstrate the uniqueness of  $\text{Li}_4\text{OSe}$ , we further compare the phonon dispersion of  $\text{Li}_4\text{OSe}$  and the antifluorite  $\text{Li}_2\text{Se}$  along the same direction in Fig. 3(b). Unlike  $\text{Li}_2\text{Se}$ , there is no *a-o* gap in  $\text{Li}_4\text{OSe}$ , which always disallows *aa* scattering. Meanwhile, the much larger optical bandwidth in  $\text{Li}_4\text{OSe}$  indicates a stronger interaction of one acoustic phonon with two optical phonons (*aa* scattering), as the bandwidth of optical bunching determines the phase space of *aa* scattering [12]. This phonon comparison suggests that  $\text{Li}_4\text{OSe}$  has a lower  $\kappa_l$  value than  $\text{Li}_2\text{Se}$  ( $14.9 \text{ W m}^{-1} \text{ K}^{-1}$ ) [12].

In order to illustrate the phonon transport properties of  $\text{Li}_4\text{OSe}$ , the frequency dependence of the phonon scattering rate and group velocities are calculated. First of all, Fig. 4(a) shows the scattering rate of phonons at 300 K. In the low-frequency range, the small DOS leads to a small phase space for three acoustic phonon (*aaa*) scattering, and the phonon energies are not enough for *aa* and *aoo* scattering, thus resulting in very weak phonon-phonon (ph-ph) interaction. Since the *a-o* coupling provides a continuous phonon spectrum without an *a-o* gap, the phase space for scattering always expands as the phonon frequency rises, and the scattering rate monotonously increases accordingly. Second, we further calculate the phonon group velocities of  $\text{Li}_4\text{OSe}$  based on phonon spectra (as shown in Fig. S3 in the Supplemental Material [36]). As reported in other thermoelectric materials like  $\text{Bi}_2\text{Te}_3$ ,  $\text{Bi}_2\text{Se}_3$ , and  $\text{Sb}_2\text{Te}_3$  [2], the heavier the atom is, the lower the group velocity is. Indeed, the acoustic phonon velocity ( $< 7.5 \text{ km s}^{-1}$ ) is relatively low in  $\text{Li}_4\text{OSe}$ . Compared with the acoustic phonon velocity, the optical phonon velocities ( $< 4 \text{ km s}^{-1}$ ) are lower as a result of the less dispersive optical phonon branches. Owing to the *a-o* coupling, there is a sharp decline in group velocity around 3 THz.

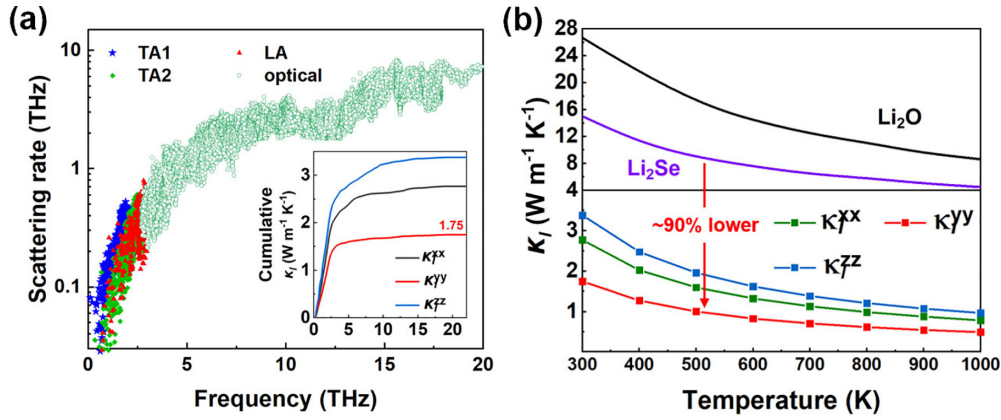


FIG. 4. (a) Frequency dependence of phonon scattering rates of  $\text{Li}_4\text{OSe}$  due to the intrinsic phonon-phonon interaction at 300 K. The inset in (a) is the cumulative lattice thermal conductivity. (b) Calculated  $\kappa_l$  versus temperature for  $\text{Li}_4\text{OSe}$  compared with  $\text{Li}_2\text{Se}$  (purple curve) and  $\text{Li}_2\text{O}$  (black curve) from Ref. [12]. The value of  $\kappa_l$  for  $\text{Li}_4\text{OSe}$  is much smaller than those for  $\text{Li}_2\text{Se}$  and  $\text{Li}_2\text{O}$  ( $\sim 90\%$  lower).

The high scattering rate and low group velocity of the heat-carrying acoustic phonon indicate a low lattice thermal conductivity in  $\text{Li}_4\text{OSe}$ . The cumulative  $\kappa_l$  at 300 K in Fig. 4(a) shows that the value of  $\kappa_l$  in the  $y$  direction is as low as  $1.75 \text{ W m}^{-1} \text{ K}^{-1}$ , even though there is a large number of light atoms, i.e., O and Li atoms, in the crystal. According to the plot of cumulative  $\kappa_l$ , the acoustic phonons at 0–3 THz contribute most of the thermal conductivity, resulting from the limited phase space for scattering. As the phonon frequency exceeds 3 THz, the rate of accumulation suddenly slows down because of the sharply decreasing phonon velocities caused by the  $a$ - $o$  coupling as well as the increasing phonon scattering rate.

Figure 4(b) gives the calculated  $\kappa_l$  of  $\text{Li}_4\text{OSe}$  as a function of temperature in comparison with  $\text{Li}_2\text{Se}$  and  $\text{Li}_2\text{O}$ . As the temperature arises, the phonon scattering is enhanced significantly; therefore, the values of  $\kappa_l$  at 1000 K are much lower than that at room temperature. Since the acoustic phonons, dominated by heavy elements, contribute most of the thermal conductivity,  $\text{Li}_2\text{Se}$  with slower velocity acoustic phonons provides lower  $\kappa_l$  than  $\text{Li}_2\text{O}$ . Meanwhile, the values of  $\kappa_l$  for  $\text{Li}_4\text{OSe}$  range from  $1.75 \text{ W m}^{-1} \text{ K}^{-1}$  at 300 K to  $0.49 \text{ W m}^{-1} \text{ K}^{-1}$  at 1000 K [shown in Fig. 4(b)]. On the one hand, such a small  $\kappa_l$  is comparable to those of the traditional TE materials consisting of heavy elements, for example,  $1.2 \text{ W m}^{-1} \text{ K}^{-1}$  for  $\text{Bi}_2\text{Te}_3$ ,  $1.9 \text{ W m}^{-1} \text{ K}^{-1}$  for  $\text{Sb}_2\text{Te}_3$ , and  $3.1 \text{ W m}^{-1} \text{ K}^{-1}$  for  $\text{Bi}_2\text{Se}_3$  at room temperature [2]. On the other hand,  $\text{Li}_4\text{OSe}$  gives much smaller values of  $\kappa_l$  than  $\text{Li}_2\text{Se}$  (an astonishing  $\sim 90\%$  lower), showing that our strategy can reduce the lattice thermal conductivity more significantly in antiperovskites than other approaches like twisting [46] and doping [47]. This result suggests that light and heavy element composite materials can also demonstrate a quite low lattice thermal conductivity.

### C. Soft optical phonon modes

The projected density of states (PDOS) in Fig. 3(a) reveals that the medium-frequency optical phonon modes occupying the  $a$ - $o$  gap are dominated by both O and Li atoms. These modes are caused by two factors: (i) the softening of high-

frequency optical phonon modes dominated by Li atoms and (ii) the medium-frequency vibrations of O atoms, whose mass is between those of Li and Se atoms. Since the PDOS in the middle-frequency region is mainly determined by Li atoms, it thus clearly indicates that the softening of high-frequency optical phonons is the most significant factor in  $\text{Li}_4\text{OSe}$ .

To rationalize the soft optical phonon modes in  $\text{Li}_4\text{OSe}$ , we construct a hypothetical “asymmetric  $\text{Li}_2\text{Se}$ ” model with O atoms removed in the  $\text{Li}_4\text{OSe}$  crystal lattice (see Fig. S5(a) in the Supplemental Material [36]) or some of the Li atoms moved artificially in the  $\text{Li}_2\text{Se}$  crystal, similar to the Li-Se bond in  $\text{Li}_4\text{OSe}$ . Surprisingly, the soft optical phonon modes appear in the constructed asymmetric  $\text{Li}_2\text{Se}$ , which is quite different from symmetric  $\text{Li}_2\text{Se}$ . We further use a simpler asymmetric  $\text{Li}_2\text{Se}$  model with only one Li atom shifted along the  $y$  axis [see Fig. 5(a)] and observe an obvious soft mode (the red optical phonon branch). The soft mode mainly comes from the shifted Li atom (see Fig. 5(b) and also Figs. S5(b) and 5(c) in the Supplemental Material [36]); therefore, we project a phonon band structure into the atomic motion of the Li atom that is moved along the  $x$ ,  $y$ , and  $z$  directions in Fig. S6 in the Supplemental Material [36] and find that the behavior of the optical branches is similar to the crystal-field splitting in the asymmetry lattice. We thus speculate that it is the symmetry breaking that leads to the large splitting of optical phonon bands and the softening of optical phonon modes. The same phenomenon is also found in the  $\text{Na}_2\text{Se}$  crystal (see Fig. S7), suggesting that the optical phonon splitting is normal in the asymmetric antiperovskite structure.

To reveal the mechanism of the optical phonon band splitting, we construct a Wannier TB phonon Hamiltonian, and the  $x$ ,  $y$ , and  $z$  components for each atomic site can be viewed as three localized  $p$  orbitals in three-dimensional space [27]. With the symmetry breaking, the on-site energy  $E_{\text{on-site}}$  of the Li atom in symmetric  $\text{Li}_2\text{Se}$  [black line in Fig. 5(c)] is split onto the lowest- and highest-frequency phonon branches in asymmetric  $\text{Li}_2\text{Se}$  (blue lines). The splitting of  $E_{\text{on-site}}$  can be regarded as the hybridization of localized  $p$  orbitals of the Li atom, further leading to softening of the optical mode. When the first- (yellow lines), second- (green lines), and full-neighbor (red lines) interactions of Li atoms are taken

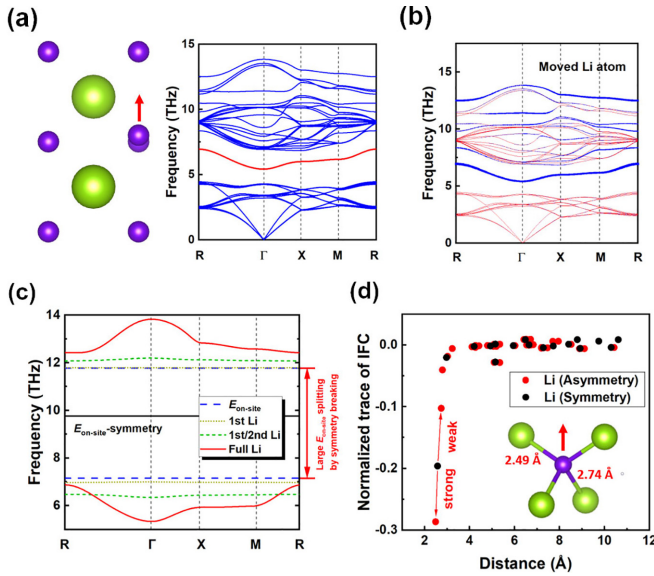


FIG. 5. (a) Crystal structure of asymmetric Li<sub>2</sub>Se with only one Li atom moved (left) and its phonon spectra (right). An obvious soft optical branch appears in the *a-o* gap (red curve). (b) Projected band structure of the Li atom that moved (blue curve). The projections of other atoms are given in Figs. S5(b) and S5(c) in the Supplemental Material [36]. The soft optical mode is mainly dominated by the Li atoms that moved. (c) The lowest- and highest-frequency optical branches of the asymmetric Li<sub>2</sub>Se, showing the band splitting due to the lattice symmetry breaking. The colored lines represent the dispersions with the inclusion of the on-site energy splitting, as well as the first-, second-, and full-neighbor interactions of Li atoms, compared with the on-site energy of symmetric Li<sub>2</sub>Se (black curve). (d) Normalized traces of IFCs for the Li atom in symmetric and asymmetric Li<sub>2</sub>Se (black and red dots).

into account, the soft optical phonon band becomes dispersive in Fig. 5(c), while the band splitting is almost unchanged. This result indicates that the optical phonon band splitting mainly derives from the change in  $E_{\text{on-site}}$ , which could be related to the redistribution of charge near the shifted Li atom in asymmetric Li<sub>2</sub>Se.

To study the effect of charge redistribution in simple asymmetric Li<sub>2</sub>Se, we calculate the normalized traces of harmonic interatomic force constants (IFCs) [8] for the Li atom that moved versus the interaction distance in Fig. 5(d). Because the degeneracy of Li-Se bonds is removed in the asymmetric lattice, there is a large difference between the two sets of IFCs at a distance of 2.6 Å, which can be viewed as the splitting in IFCs. When the distance is larger than 3 Å, there is nearly no difference in IFCs between the symmetric and asymmetric models. Therefore, the symmetry breaking modifies only the local IFC values. Such local interactions are also observed in Li<sub>4</sub>OSe (see Fig. S9 in the Supplemental Material [36]). This means that the short-range charge redistribution in real space is the physical origin for the splitting of on-site energies, which leads to optical branch softening. The short-range charge redistribution can be realized by lowering the lattice symmetry, such as with the split-anion approach, doping, alloys, twisting, and so on. This picture of soft optical phonon modes is universal and can be extended to other materials with light atoms and a large *a-o* gap. For instance, using

the split-anion approach, the lattice thermal conductivity of Li<sub>4</sub>OSe (1.06 W m<sup>-1</sup> K<sup>-1</sup>) is an order of magnitude lower than that of Li<sub>2</sub>Te (12.5 W m<sup>-1</sup> K<sup>-1</sup>).

#### D. Electronic structure, the electrical transport property, and the power factor

A remarkable feature of the band structure of Li<sub>4</sub>OSe (Fig. S12(a) in the Supplemental Material [36]) is that there are several local maxima of the valence bands at points  $\Gamma$  (0, 0, 0), *D* (0, 0.5, 0.5), and *E* (-0.5, 0.5, 0.5), with the energy difference being smaller than 0.07 eV. The flat band along  $\Gamma$ -*D*-*E* indicates a type of Van Hove singularity, resulting in a peak in the DOS around the valence band maximum (VBM). High valley multiplicity and strong anisotropic valence band dispersion suggest good thermoelectric performance [48–50].

Because of the high valley multiplicity around the valence band, we focus on *p*-type Li<sub>4</sub>OSe and calculate its carrier lifetimes (Fig. S12(b) in the Supplemental Material [36]) by using the QUANTUM ESPRESSO and EPW codes [33,34]. The lifetime decreases rapidly as the holes away from the VBM because the increasing phase space enhances the scattering and hole transitions. As a result, the carrier lifetime cannot be simply approximated to the one at the VBM for *p*-type Li<sub>4</sub>OSe, which would overestimate the conductivity and the ultimate *ZT* value. The power factor (PF) of *p*-type Li<sub>4</sub>OSe as a function of carrier concentration in the *y* direction at 300–1000 K is given in Fig. S12(c) in the Supplemental Material [36]. The optimized PFs retain high values at 300–1000 K ( $\sim 1.25$  mW m<sup>-1</sup> K<sup>-2</sup>), comparable to those in Bi<sub>2</sub>Te<sub>3</sub> ( $\sim 3.5$  mW m<sup>-1</sup> K<sup>-2</sup>) under the optimal hole density [51]. Indeed, we have not considered the ionized impurity scattering in doped Li<sub>4</sub>OSe for simplicity, which may cause an overestimate of the PF values. Owing to the increasing collision cross section of fixed charges, the ionized impurity scattering is known to be more important at low temperatures [52]. Conversely, *e*-ph scattering is dominant at high temperatures due to stronger lattice vibration. Therefore, we believe that the influence of scattering with ionized dopants in Li<sub>4</sub>OSe at high temperatures is relatively less significant, and the overestimation of the average PF from room temperature to high temperature (PF<sub>avg</sub>) will not exceed an order of magnitude. In addition, the strength of the ionized impurity scattering at low temperature can be reduced by doping transition-metal elements [53]. These desirable electronic properties suggest that *p*-type Li<sub>4</sub>OSe could demonstrate a very promising TE performance.

#### E. Reduction of lattice thermal conductivity by *e*-ph interaction

Although the effect of *e*-ph interaction on phonon transport was usually ignored in previous studies, it sometimes significantly modifies the lattice thermal conductivity. For instance, the *e*-ph interaction reduces the lattice thermal conductivity of *p*-type silicon by 45% at room temperature as the carrier concentration exceeds 10<sup>19</sup> cm<sup>-3</sup> [54]. Therefore, we discuss the effect of *e*-ph interaction on the lattice thermal conductivity of *p*-type Li<sub>4</sub>OSe. We first estimate the best concentration in *p*-type Li<sub>4</sub>OSe in Fig. S12(d) in the Supplemental

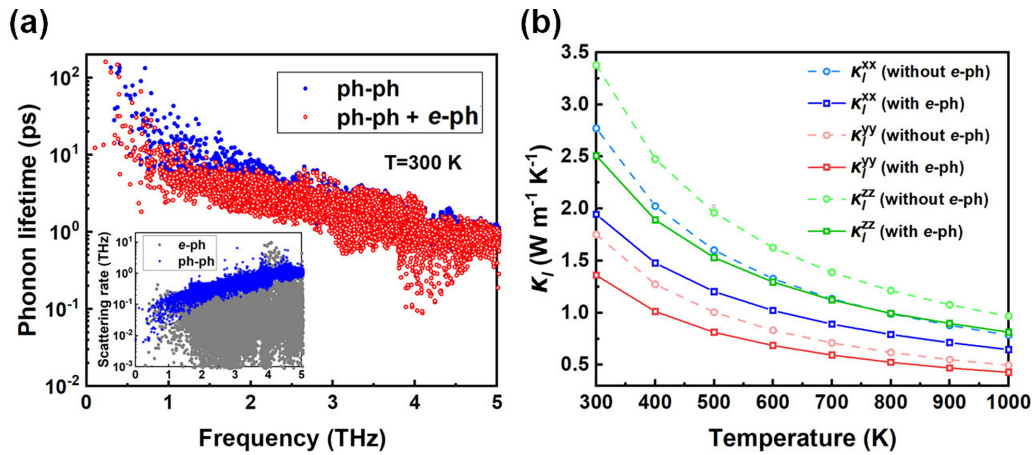


FIG. 6. (a) Frequency dependence of phonon lifetimes for *p*-type  $\text{Li}_4\text{OSe}$  at a carrier concentration of  $5 \times 10^{20} \text{ cm}^{-3}$  without (blue) and with (red) *e*-ph interaction. The inset in (a) is the phonon scattering rate in *p*-type  $\text{Li}_4\text{OSe}$  due to the *e*-ph interaction (gray dots) and the intrinsic ph-ph interaction (blue dots). (b) Lattice thermal conductivity versus the temperature for  $\text{Li}_4\text{OSe}$  at a carrier concentration of  $5 \times 10^{20} \text{ cm}^{-3}$  without (dashed lines) and with (solid lines) *e*-ph interaction.

Material [36]. It is found that  $5 \times 10^{20} \text{ cm}^{-3}$  is the best carrier concentration for *p*-type  $\text{Li}_4\text{OSe}$ , and we will calculate all data at this carrier concentration in this section. Figure 6(a) gives the phonon lifetimes of *p*-type  $\text{Li}_4\text{OSe}$  with (red dots) and without (blue dots) *e*-ph interactions. When the phonon frequency is larger than 2.5 THz, the two lifetimes are almost the same because the *e*-ph interaction scattering rates here are nearly 1–2 orders of magnitude lower than the intrinsic ph-ph ones. As the *e*-ph interaction scattering rates surpass the ph-ph scattering rates for some low-frequency phonons, the lifetimes of these phonons obviously decrease. This is expected to have a significant impact on phonon transport because most of the heat is carried by the phonons with the lowest frequencies. The scattering rates and phonon lifetimes at 1000 K are also provided in Fig. S13 in the Supplemental Material [36], which shows increasing phonon scatterings for both the *e*-ph and ph-ph interactions. Meanwhile, the temperature has a larger influence on ph-ph interactions than *e*-ph interactions in *p*-type  $\text{Li}_4\text{OSe}$  [see Figs. 6(a) and S13].

Figure 6(b) shows the calculated lattice thermal conductivity of *p*-type  $\text{Li}_4\text{OSe}$  without (dashed line) and with (solid line) *e*-ph interactions. Because of the *e*-ph interaction in the heavily doped region, the values of  $\kappa_l$  of *p*-type  $\text{Li}_4\text{OSe}$  are lower than those in the intrinsic  $\text{Li}_4\text{OSe}$ . Moreover, this reduction weakens with increasing temperature due to the larger temperature dependence of ph-ph interactions. For instance, the *e*-ph interaction reduces  $\kappa_l$  along the *y* axis by 22.2% at 300 K and 15.2% at 1000 K. This reduction is smaller than the value of 45% in Si [54] and 60% in SiGe alloys [55] as a result of the relatively larger ph-ph scattering rate in  $\text{Li}_4\text{OSe}$ . The ionized impurity scattering can also affect the thermal transport at low temperatures by reducing the lattice thermal conductivity [56,57]. However, phonon scattering is the main scattering mechanism for the lattice thermal conductivity at high temperature [58,59]. Therefore, we do not consider the effect of impurity scattering on the lattice thermal conductivity in the high-temperature TE material  $\text{Li}_4\text{OSe}$ . Finally, the impact of *e*-ph interactions on  $\kappa_l$  is still non-negligible, in a range that is of great technological relevance for TE applications.

#### IV. CONCLUSION

In summary, we investigated the impairment of the thermal transport capacity with the antiferroelectric  $\text{Li}_2\text{Se}$  transforming to the quasiantiferroelectric  $\text{Li}_4\text{OSe}$  and how their  $\kappa_l$  are modulated by the split-anion approach. Our result shows that lattice symmetry breaking through the split-anion approach causes an ultralow  $\kappa_l$  by softening the optical phonon, which significantly enhances the phonon scattering. Thus, ultralow  $\kappa_l$  values, ranging from  $1.75 \text{ W m}^{-1} \text{ K}^{-1}$  at 300 K to  $0.49 \text{ W m}^{-1} \text{ K}^{-1}$  at 1000 K, can be obtained, comparable to the traditional TE materials, even though  $\text{Li}_4\text{OSe}$  has a large mass mismatch among atoms. Based on the asymmetric  $\text{Li}_2\text{Se}$  model, we uncovered the relationship between the soft optical phonon modes and the lattice symmetry breaking, in which the latter modifies a short-range redistribution of charge in real space, rendering a large band splitting of optical branches. We further demonstrated the effect of *e*-ph interactions in heavily doped  $\text{Li}_4\text{OSe}$ , which reduce  $\kappa_l$  by 15%–22% at 300–1000 K. This picture can be extended to other quasiantiferroelectrics and similar light-atom compounds, and it will stimulate intense interest in the exploration of compounds with a large mass mismatch among constituent atoms for new environmentally friendly and low-cost thermoelectric materials.

#### ACKNOWLEDGMENTS

This work was supported by the National Key Research and Development Program of China (Grant No. 2017YFA0206303, MOST of China), the National Natural Science Foundation of China (Grants No. 11474012, No. 12104421, No. 11404013, No. 61734001, and No. 61521004), the Zhejiang Provincial Natural Science Foundation of China (Grant No. LY23A040005), the Knowledge In-novation Program of Wuhan-Shuguang Project (Grant No. 2022010801020214), the China Postdoctoral Science Foundation (Grant No. 2022M712965), and the “CUGScholar” Scientific Research Funds at China University of Geosciences (Wuhan; Project No. 2021032). We used the computational resources of the Explorer 100 cluster system

of the Tsinghua National Laboratory for Information Science and Technology, and part of the analysis was performed on the

Computing Platform of the Center for Life Science of Peking University.

- [1] G. Slack, *J. Phys. Chem. Solids* **34**, 321 (1973).
- [2] T. Fang, X. Li, C. Hu, Q. Zhang, J. Yang, W. Zhang, X. Zhao, D. J. Singh, and T. Zhu, *Adv. Funct. Mater.* **29**, 1900677 (2019).
- [3] C. Chang and L.-D. Zhao, *Mater. Today Phys.* **4**, 50 (2018).
- [4] D. T. Morelli, V. Jovovic, and J. P. Heremans, *Phys. Rev. Lett.* **101**, 035901 (2008).
- [5] E. J. Skoug and D. T. Morelli, *Phys. Rev. Lett.* **107**, 235901 (2011).
- [6] W. Qiu, L. Xi, P. Wei, X. Ke, J. Yang, and W. Zhang, *Proc. Natl. Acad. Sci. USA* **111**, 15031 (2014).
- [7] O. Delaire, J. Ma, K. Marty, A. May, M. McGuire, M.-H. Du, D. Singh, A. Podlesnyak, G. Ehlers, M. Lumsden, and B. Sales, *Nat. Mater.* **10**, 614 (2011).
- [8] S. Lee, K. Esfarjani, T. Luo, J. Zhou, Z. Tian, and G. Chen, *Nat. Commun.* **5**, 3525 (2014).
- [9] J.-Y. Raty, M. Schumacher, P. Golub, V. L. Deringer, C. Gatti, and M. Wuttig, *Adv. Mater.* **31**, 1806280 (2019).
- [10] Y. Touloukian, R. Powell, C.-Y. Ho, and P. Klemens, *Thermal Conductivity: Metallic Elements and Alloys* (IFI/Plenum, New York, 1970).
- [11] A. Alofi and G. P. Srivastava, *Phys. Rev. B* **87**, 115421 (2013).
- [12] S. Mukhopadhyay, L. Lindsay, and D. S. Parker, *Phys. Rev. B* **93**, 224301 (2016).
- [13] L. Lindsay, D. A. Broido, and T. L. Reinecke, *Phys. Rev. B* **88**, 144306 (2013).
- [14] T. Takahashi and T. Kikuchi, *J. Nucl. Mater.* **91**, 93 (1980).
- [15] G. Kresse and J. Furthmüller, *Comput. Mater. Sci.* **6**, 15 (1996).
- [16] G. Kresse and J. Furthmüller, *Phys. Rev. B* **54**, 11169 (1996).
- [17] P. E. Blöchl, *Phys. Rev. B* **50**, 17953 (1994).
- [18] J. P. Perdew, K. Burke, and M. Ernzerhof, *Phys. Rev. Lett.* **77**, 3865 (1996).
- [19] H. J. Monkhorst and J. D. Pack, *Phys. Rev. B* **13**, 5188 (1976).
- [20] W. Li, J. Carrete, N. A. Katcho, and N. Mingo, *Comput. Phys. Commun.* **185**, 1747 (2014).
- [21] R. K. Kremer, K. Graf, M. Cardona, G. G. Devyatikh, A. V. Gusev, A. M. Gibin, A. V. Inyushkin, A. N. Taldenkov, and H.-J. Pohl, *Solid State Commun.* **131**, 499 (2004).
- [22] A. Togo and I. Tanaka, *Scr. Mater.* **108**, 1 (2015).
- [23] W. Li, L. Lindsay, D. A. Broido, D. A. Stewart, and N. Mingo, *Phys. Rev. B* **86**, 174307 (2012).
- [24] D. Alfè, *Comput. Phys. Commun.* **180**, 2622 (2009).
- [25] Q. Wu, S. Zhang, H.-F. Song, M. Troyer, and A. A. Soluyanov, *Comput. Phys. Commun.* **224**, 405 (2018).
- [26] J. C. Slater and G. F. Koster, *Phys. Rev.* **94**, 1498 (1954).
- [27] Y. Liu, Y. Xu, S.-C. Zhang, and W. Duan, *Phys. Rev. B* **96**, 064106 (2017).
- [28] W. H. Han, and K. J. Chang, [arXiv:1903.05286](https://arxiv.org/abs/1903.05286) (2019).
- [29] G. Samsonidze and B. Kozinsky, *Adv. Energy Mater.* **8**, 1800246 (2018).
- [30] P. Graziosi, Z. Li, and N. Neophytou, *Comput. Phys. Commun.* **287**, 108670 (2023).
- [31] J. Bardeen and W. Shockley, *Phys. Rev.* **80**, 72 (1950).
- [32] F. Giustino, M. L. Cohen, and S. G. Louie, *Phys. Rev. B* **76**, 165108 (2007).
- [33] P. Giannozzi *et al.*, *J. Phys.: Condens. Matter* **21**, 395502 (2009).
- [34] S. Poncé, E. Margine, C. Verdi, and F. Giustino, *Comput. Phys. Commun.* **209**, 116 (2016).
- [35] F. Giustino, *Rev. Mod. Phys.* **89**, 015003 (2017).
- [36] See Supplemental Material at <http://link.aps.org/supplemental/10.1103/PhysRevB.107.205206> for calculation method, XRD pattern, structural stability, convergence test, and TE performance, which includes Refs. [8,20–35,37,40–42,44].
- [37] G. K. Madsen and D. J. Singh, *Comput. Phys. Commun.* **175**, 67 (2006).
- [38] K. Persson, Materials Data on Li<sub>2</sub>Se (sg:225) by Materials Project (2020), doi: [10.17188/1199025](https://doi.org/10.17188/1199025).
- [39] K. Momma and F. Izumi, *J. Appl. Crystallogr.* **44**, 1272 (2011).
- [40] S. Nosé, *J. Chem. Phys.* **81**, 511 (1984).
- [41] W. G. Hoover, *Phys. Rev. A* **31**, 1695 (1985).
- [42] W. G. Hoover, A. J. C. Ladd, and B. Moran, *Phys. Rev. Lett.* **48**, 1818 (1982).
- [43] D. J. Evans, *J. Chem. Phys.* **78**, 3297 (1983).
- [44] A. Togo, L. Chaput, I. Tanaka, and G. Hug, *Phys. Rev. B* **81**, 174301 (2010).
- [45] K. Persson, Materials Data on Li<sub>2</sub>O (sg:225) by Materials Project (2020), doi: [10.17188/1194803](https://doi.org/10.17188/1194803).
- [46] J. Sun, M. Hu, C. Zhang, L. Bai, C. Zhang, and Q. Wang, *Adv. Funct. Mater.* **32**, 2209000 (2022).
- [47] O. Zapata-Arteaga, A. Perevedentsev, S. Marina, J. Martin, J. S. Reparaz, and M. Campoy-Quiles, *ACS Energy Lett.* **5**, 2972 (2020).
- [48] Y. Pei, X. Shi, A. Lalonde, H. Wang, L. Chen, and G. J. Snyder, *Nature (London)* **473**, 66 (2011).
- [49] Y. Tang, Z. M. Gibbs, L. A. Agapito, G. Li, H.-S. Kim, M. B. Nardelli, S. Curtarolo, and G. J. Snyder, *Nat. Mater.* **14**, 1223 (2015).
- [50] K. Peng, Z. Zhou, H. Wang, H. Wu, J. Ying, G. Han, X. Lu, G. Wang, X. Zhou, and X. Chen, *Adv. Funct. Mater.* **31**, 2100583 (2021).
- [51] X. Tang, Z. Li, W. Liu, Q. Zhang, and C. Uher, *Interdiscip. Mater.* **1**, 88 (2022).
- [52] M. Forster, A. Cuevas, E. Fourmond, F. E. Rougieux, and M. Lemitte, *J. Appl. Phys.* **111**, 043701 (2012).
- [53] J. Mao, J. Shuai, S. Song, Y. Wu, R. Dally, J. Zhou, Z. Liu, J. Sun, Q. Zhang, C. dela Cruz, S. Wilson, Y. Pei, D. J. Singh, G. Chen, C.-W. Chu, and Z. Ren, *Proc. Natl. Acad. Sci. USA* **114**, 10548 (2017).
- [54] B. Liao, B. Qiu, J. Zhou, S. Huberman, K. Esfarjani, and G. Chen, *Phys. Rev. Lett.* **114**, 115901 (2015).
- [55] Q. Xu, J. Zhou, T.-H. Liu, and G. Chen, *Appl. Phys. Lett.* **115**, 023903 (2019).
- [56] W. Kim, F. Marsiglio, and J. P. Carbotte, *Phys. Rev. B* **68**, 174513 (2003).
- [57] A. V. Sologubenko, N. D. Zhigadlo, J. Karpinski, and H. R. Ott, *Phys. Rev. B* **74**, 184523 (2006).
- [58] A. AlShaikhi, S. Barman, and G. P. Srivastava, *Phys. Rev. B* **81**, 195320 (2010).
- [59] L. Pan, S. Mitra, L.-D. Zhao, Y. Shen, Y. Wang, C. Felser, and D. Berardan, *Adv. Funct. Mater.* **26**, 5149 (2016).